

1 **Impact of grids and dynamical cores in CESM2.2 on**
2 **the surface mass balance of the Greenland Ice Sheet**

3 **Adam R. Herrington** ¹, **Marcus Lofverstrom** ², **Peter H. Lauritzen** ¹ and
4 **Andrew Gettelman** ¹

5 ¹National Center for Atmospheric Research, 1850 Table Mesa Drive, Boulder, Colorado, USA
6 ²Department of Geosciences, University of Arizona, 1040 E. 4th Street, Tucson, AZ USA

7 **Key Points:**

- 8 • enter point 1 here
9 • enter point 2 here
10 • enter point 3 here

Abstract

[enter your Abstract here]

Plain Language Summary

[enter your Plain Language Summary here or delete this section]

1 Introduction

General Circulation Models (GCMs) are powerful tools for understanding the meteorology and climate of the high-latitudes, which are among the most sensitive regions on Earth to global and environmental change. Despite their importance, the numerical treatment of polar regions in GCMs is handled in vastly-different ways due to the so-called *pole-problem* (D. Williamson, 2007), which refers to numerical instability arising from the convergence of meridians to polar singularities on latitude-longitude grids (e.g., Figure 1a). Depending on the numerics, methods exist to suppress this instability, and latitude-longitude grids may be advantageous for polar processes as structures can be represented with more degrees of freedom than elsewhere in the computational domain. With the recent trend towards globally uniform unstructured grids, any potential benefits of latitude-longitude grids on polar regions may become a relic of the past. In this study, a spectrum of model grids and dynamical cores (hereafter referred to as *dycores*) available in the Community Earth System Model, version 2.2 (CESM; <http://www.cesm.ucar.edu/models/cesm2/>) are evaluated to understand their impacts on the simulated characteristics of the Arctic, with a special focus on the meteorology over the Greenland Ice Sheet.

In the 1970's the pole problem was largely defeated through wide-spread adoption of efficient spectral transform methods in GCMs. These methods transform grid point fields into a global, isotropic representation in wave space, where linear operators (e.g. horizontal derivatives) in the equation set can be solved for exactly. While spectral transform methods are still used in the 21st century, local numerical methods have become desirable for their ability to run efficiently on massively parallel systems. The pole-problem has thus re-emerged in contemporary climate models that use latitude-longitude grids, and some combination of reduced grids and polar filters are necessary to ameliorate this instability (Jablonowski & Williamson, 2011). Polar filters are akin to a band-aid; they subdue the growth of unstable modes by applying additional damping to the solution over polar regions. One might expect that this additional damping reduces the effective resolution such that the resolved scales are similar across the entire domain, but this seems unlikely (describe why) and is explored further in this study.

An alternative approach is to use unstructured grids, which allow for more flexible grid structures that permit quasi-uniform grid spacing globally and eliminates the pole-problem entirely (e.g., Figure 1c). This grid flexibility also allows for variable-resolution or regional grid refinement (e.g., Figure 2). Grids can be developed with refinement over polar regions that could in principle make up for any loss in polar resolution in transitioning away from latitude-longitude grids (e.g., Figure 2), although this comes at the cost of a smaller CFL-limiting time-step in the refined region (the CFL-condition — short for Courant–Friedrichs–Lowy condition — is a necessary condition for numerical stability when using discrete data in time and space). However, unstructured grids scale more efficiently on parallel systems than latitude-longitude grids, likely resulting in a greater prevalence of unstructured grids as computing power continued to increase over time.

The meteorology and climate of the Arctic is characterized by a range of processes and scales that are difficult to represent in GCMs (Bromwich et al., 2001; Smirnova & Golubkin, 2017; van Kampenhout et al., 2018). For example, while synoptic scale storms

are generally well represented at typical GCM resolutions of 1 to 2 degrees (Jablonowski & Williamson, 2006; Stocker, 2014), mesoscale Polar Lows are not well resolved at these resolutions. These mesoscale systems are prevalent during the cold season and produce gale-force winds that can induce large heat and moisture fluxes through the underlying sea-ice/ocean interface. The Arctic also contains the Greenland Ice Sheet (hereafter denoted as *GrIS*). While it blankets the largest island in the world (Greenland), many of the processes that control the *GrIS* annual surface mass balance (the integrated sum of precipitation and melting) are only partially resolved at typical GCM resolutions. For example, *GrIS* precipitation is typically confined to the ice-sheet margins (predominately the southeastern margin) where orographic precipitation is generated by steep topographic slopes. Moreover, *GrIS* ablation areas (marginal regions where seasonal melting exceeds the annual mass input from precipitation) are typically 10s to 100 km wide and confined to low-level areas or regions with limited precipitation. GCMs struggle to resolve the magnitude and extent of these features (van Kampenhout et al., 2018), which can lead to unrealistic ice sheet growth in models with an interactive ice sheet component (e.g., Lofverstrom et al., 2020).

The goal of this study is to characterize the representation of high-latitude regions using the spectral-element and finite-volume dycores in CESM2.2, as these models treat the high-latitudes, e.g., the pole-problem, in different ways. The manuscript is laid out as follows: Section 2 consists of documentation of the grids, dycores and physical parameterizations used in this study. The Arctic refined grids were developed by the authors, and this section serves as their official documentation in CESM2.2. Section 2 also contains a description of the experiments along with reanalysis datasets and post-processing software used for evaluating the model simulations. Section 3 contains the results of the experiments, followed by Section 4 that provides a general discussion and conclusions.

2 Methods

2.1 Dynamical cores

The atmospheric component of CESM2.2, the Community Atmosphere Model, version 6.3 (CAM; <https://ncar.github.io/CAM/doc/build/html/index.html>), supports a number of different atmospheric dynamical cores. These include dycores using latitude-longitude grids, such as finite-volume (FV; Lin, 2004) and eulerian spectral transform (EUL; Collins et al., 2006) models, and dycores built on unstructured grids, including spectral-element (SE; Lauritzen et al., 2018) and finite-volume 3 (FV3; Putman & Lin, 2007) models. The EUL dycore is the oldest dycore in CAM, and the least supported of all the dycores in the current model. FV3 is the newest dycore in CAM, but it was not fully incorporated at the time this work commenced; both the EUL and FV3 dycores are omitted from this study. As such, the results presented in this study are comparing the performance of the SE and FV dycores.

2.1.1 Finite-volume (FV) dynamical core

The FV dycore is a hydrostatic model that integrates the equations of motion using a finite-volume discretization on a spherical latitude-longitude grid (Lin & Rood, 1997). The 2D dynamics evolve in floating Lagrangian layers that are periodically mapped to Eulerian reference grid in the vertical (Lin, 2004), using a hybrid-pressure vertical coordinate. Hyperviscous damping is applied to the divergent modes while Laplacian damping is applied to momentum in the top few layers, referred to as a *sponge layer* (Lauritzen et al., 2011). A polar filter is used to avoid computational instability due to the convergence of the meridians, allowing for a more practical time-step. It takes the form of a Fourier filter in the zonal direction, with the damping coefficients increasing monotonically in the poleward direction (Suarez & Takacs, 1995).

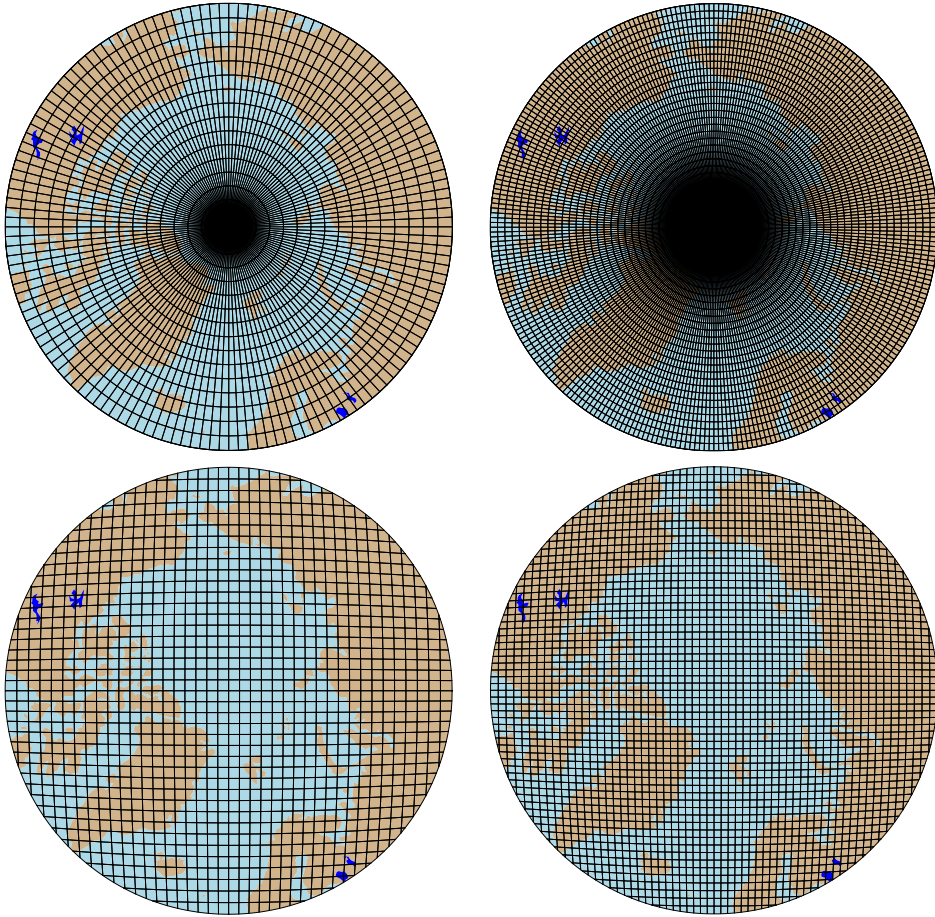


Figure 1. Computational grids for the uniform $1^\circ - 2^\circ$ grids in this study.

108 **2.1.2 Spectral-element (SE) dynamical core**

109 The SE dycore is a hydrostatic model that integrates the equations of motion us-
 110 ing a high-order continuous Galerkin method (Taylor et al., 1997; Dennis et al., 2012).
 111 The computational domain is a cubed-sphere grid tiled with quadrilateral elements (e.g.,
 112 Figure 2). Each element contains a fourth order basis set in each horizontal direction,
 113 with the solution defined at the roots of the basis functions, the Gauss-Lobatto-Legendre
 114 (GLL) quadrature points. This results in 16 GLL nodal points within each element, with
 115 12 of the points lying on the (shared) element boundary. Communication between el-
 116 ements happens via the direct stiffness summation (Canuto et al., 2007), which applies
 117 a numerical flux to the element boundaries that reconciles overlapping nodal values and
 118 produces a continuous global basis set.

119 As with the FV dycore, the dynamics evolve in floating Lagrangian layers that are
 120 subsequently mapped to an Eulerian reference grid. A dry mass vertical coordinate was
 121 more recently implemented for thermodynamic consistency with condensates (Lauritzen
 122 et al., 2018). The 2D dynamics have no implicit dissipation and so hyperviscosity op-
 123 erators are applied to all prognostic variables to remove spurious numerical errors (Dennis
 124 et al., 2012). Laplacian damping is applied in the sponge layer.

125 The SE dycore supports regional grid refinement via its variable-resolution config-
 126 uration, requiring two enhancements over uniform resolution grids. (1) As the numer-



Figure 2. Spectral-element grid for the variable-resolution ARCTIC grid in this study. Note that this is not the computational grid; each element has 3×3 independent grid points.

ical viscosity increases with resolution, explicit hyperviscosity relaxes according to the local element size, reducing in strength by about an order of magnitude per halving of the grid spacing. A tensor-hyperviscosity formulation is used (Guba et al., 2014), which adjusts the coefficients in two orthogonal directions to more accurately target highly distorted quadrilateral elements. (2) The topography boundary conditions need to be smoothed in a way that does not excite grid scale modes, and so the NCAR topography software (Lauritzen et al., 2015) was modified to scale the smoothing radius by the local element size.

For spectral-element grids with quasi-uniform grid spacing, a variant in which tracer advection is computed using the Conservative Semi-Lagrangian Multi-tracer transport scheme (CSLAM) is used instead (Lauritzen et al., 2017). CSLAM has improved tracer property preservation and accelerated multi-tracer transport. It uses a separate grid from the spectral-element dynamics, through dividing each element into 3×3 control volumes with quasi-equal area. The physical parameterizations are computed from the state on the CSLAM grid, which has clear advantages over the default SE dycore in which the physics are evaluated at the GLL nodal points (A. Herrington et al., 2018).

2.2 Grids

Six grid are evaluated in this study (Table X). The FV dycore is run with 1° and 2° grid spacing, referred to as *f09* and *f19*, respectively (Figure 1a,b). The 1° equivalent of the CAM-SE-CSLAM grid is also run, referred to as *ne30pg3* (Figure 1c), where *ne* refers to a grid with of $ne \times ne$ elements per cubed-sphere face, and *pg* denotes that there are $pg \times pg$ control volumes per element for computing the physics. An additional 1° CAM-SE-CSLAM grid is run, but with the physical parameterizations computed on a grid that contains 2×2 control volumes per element, *ne30pg2* (Figure 1d; A. R. Herrington et al., 2019).

Two variable resolution meshes were developed as part of the CESM2.2 release that contains grid refinement over the Arctic (Figure 2). The Arctic meshes were developed using the software package SQuadgen (<https://github.com/ClimateGlobalChange/squadgen>). The *ARCTIC* grid is a 1° grid with $\frac{1}{4}^\circ$ regional refinement over the broader Arctic region. The *ARCTICGRIS* grid is identical to the *ARCTIC* grid, but contains an additional patch covering the big island of Greenland with $\frac{1}{8}^\circ$ resolution.

158 2.3 Physical parameterizations

159 The CAM6 physical parameterization package (hereafter referred to as the *physics*;
 160 <https://ncar.github.io/CAM/doc/build/html/index.html>) is used for all simula-
 161 tions in this study. CAM6 physics is most noteably different from it's predecessors through
 162 the incorporation of high-order turbulence closure, Cloud Layers Unified by Binormals
 163 (CLUBB; Golaz et al., 2002; Bogenschutz et al., 2013), which jointly acts as a PBL, shal-
 164 low convection and cloud macrophysics scheme. CLUBB is coupled with the MG2 mi-
 165 crophysics scheme (Gettelman et al., 2015), with prognostic precipitation and classical
 166 nucleation theory in representing cloud ice for improved cloud-aerosol interactions. Deep
 167 convection is parameterized using a convective quasi-equilibrium mass flux scheme (Zhang
 168 & McFarlane, 1995; Neale et al., 2008) inclusing convective momentum transport (Richter
 169 et al., 2010). PBL form drag is modeled after (Beljaars et al., 2004) and orographic grav-
 170 ity wave drag is represented with an anisotropic method informed by the orientation of
 171 topographic ridges at the sub-grid scale.

172 The CAM convention is that the physics package determines the vertical resolu-
 173 tion. Since all runs use CAM6 physics, all grids and dycores use 32 levels in the verti-
 174 cal, with a model top of about 1 hPa or about 40 km. The physics time-step, in con-
 175 trast, is dependent on grid resolution. Increases in horizontal resolution permit faster
 176 vertical velocities that reduce characteristic time-scales, and so the physics time-step should
 177 be reduced to avoid large time truncation errors (A. Herrington & Reed, 2018). The *ARCTIC*
 178 and *ARCTICGRIS* grids are therefore run with a 4× and 8× reduction in physics time-
 179 step relative to the default 1800 s time-step used in coarser, uniform resolution grids.

180 Initial simulations with the *ne30pg3* spectral-element grid produced a weaker short-
 181 wave cloud forcing relative to the tuned up finite-volume dycore. All runs with the spectral-
 182 element dycore have two CLUBB parameter changes in order to provide a more realis-
 183 tic shortwave cloud forcing. These are CLUBB's *gamma* parameter, reduced from 0.308
 184 to 0.270, and *c14*, reduced from 2.2 to 1.6. Briefly, the *gamma* parameter scales the width
 185 of the sub-grid distribution of vertical velocity, and *c14* controls the strength of the damp-
 186 ing term in the equation for the horizontal component of turbulent kinetic energy. For
 187 a thorough explanation of how CLUBB parameters impact the simulated climate, the
 188 reader is referred to (Guo et al., 2015).

189 2.4 Experimental design

190 All grids and dycores are run using an identical transient 1979-1998 AMIP-style
 191 configuration, with prescribed monthly SST/sea-ice after (Hurrell et al., 2008). This con-
 192 figuration refers to the *FHIST compset* and runs out of the box in CESM2.2. The Com-
 193 munity Land Model (CLM5; [https://escomp.github.io/ctsm-docs/versions/release](https://escomp.github.io/ctsm-docs/versions/release-clm5.0/html/users_guide/index.html)
 194 -clm5.0/html/users_guide/index.html), which uses the same grid as the atmosphere
 195 grid, calculates the surface energy balance at each land tile within a grid cell, which is
 196 used to compute snow and bare ice melting to inform the surface mass balance (SMB)
 197 of a glacier unit (van Kampenhout et al., 2020a). For land ice tiles coinciding with the
 198 Antarctic and Greenland Ice Sheets, the surface energy and mass balance are evaluated
 199 at ten elevation classes, and integrated over sub-grid hypsometric area-elevation bins for
 200 more accurate estimation of the surface mass balance of the big ice sheets. Ice accumu-
 201 lation is modeled as a capping flux, or snow in excess of the assumed 10 m snow cap, and
 202 refreezing of liquid within the snowpack additionally acts as a source of mass in the SMB
 203 calculation. Since the 10 m snowcap needs to be reached in the accumulation zone to
 204 simulate the SMB, the snow depths in the variable-resolution grids were spun-up by forc-
 205 ing CLM in standalone mode, cycling over 20 years of a fully coupled *ARCTIC* run for
 206 about 500 years. The uniform resolution grids are all initialized with an SMB from an
 207 existing *f09* spun-up initial condition.

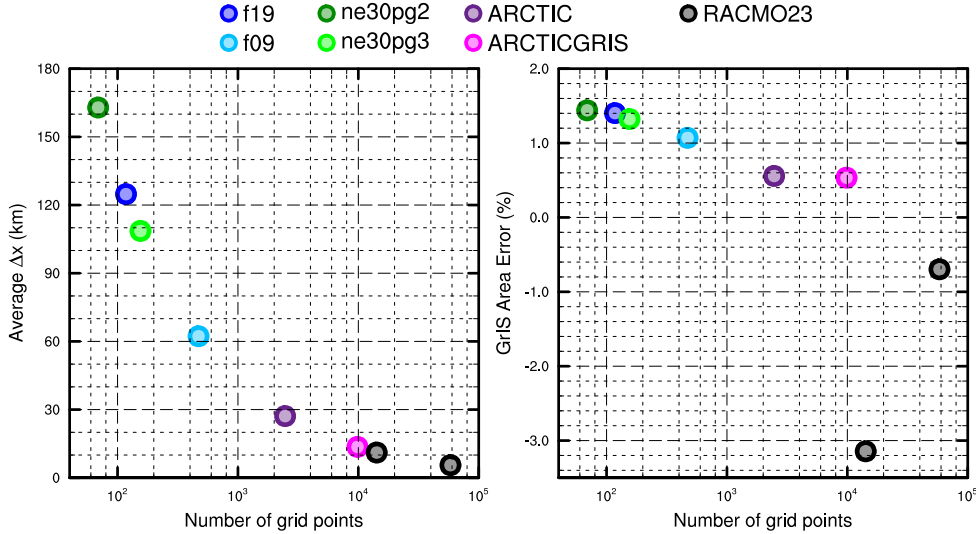


Figure 3. The spatial properties of the GrIS as represented by different grids in this study. (Left) approximate average grid spacing over GrIS, (right) GrIS area error, computed as the relative differences from a 4km dataset used to create the CESM ice masks.

208

2.5 SMB Analysis

209
210
211
212
213
214
215
216
217
218
219
220
221
222
223
224
225

The SMB is the sum of the mass source term, accumulation (i.e., precipitation), and the mass sink term, ablation. Ablation can be expressed as evaporation/sublimation plus total runoff, with runoff being a combination of liquid precipitation and snow and ice melt. Not all liquid precipitation becomes runoff; rain may penetrate pore spaces in the firn layer and freeze, forming ice lenses in the subsurface. All these processes are represented by different components in CESM, and the surface mass balance is computed by CLM. CLM uses a downscaling technique to account for sub-grid variability in SMB. In short, the ice sheet patch in a CLM grid cell is subdivided into 10 elevation classes (EC), weighted by their respective area fractions at each EC, which is derived from a high resolution GrIS elevation model. The near surface air temperature, humidity and air density are calculated at each EC using an assumed lapse rate and the elevation difference from the grid mean, allowing for the precipitation rates to be repartitioned into solid or liquid based on the temperature of each EC. This technique allows for a unique surface energy balance and surface mass balance at each EC. Integrating over all ECs using the area weights then provides a more accurate SMB. For a detailed description of how the SMB is computed in the CESM, the reader is referred to (Sellevold et al., 2019; van Kampenhout et al., 2020b).

226
227
228
229
230
231
232
233
234

Simulated SMB are compared against several observational data products. RACMO2.3 11km and RACMO2.3p2 5.5km are regional model simulations that have been forced by reanalysis at its domain boundaries. The RACMO simulations have been shown to perform very skillfully against observations and is therefore considered an ideal modeling target (Noël et al., 2015, 2019). The Land Ice Verification and Validation toolkit (LIVVkit), version 2.1 (Evans et al., 2019) maintains a repository of snow pit and ice core SMB measurements, as well as the IceBridge radar accumulation dataset. The LIVVkit dataset is compared against model simulations by finding the nearest grid cell center to the location of each observation.

A common high resolution dataset is used to generate the GrIS boundary conditions using the CLM dataset creation tools. Since we are interested in the total ice sheet SMB, we seek to integrate various components of the SMB over a common ice mask to get the total mass change of the GrIS. Figure 3 shows the GrIS ice mask area across the different grids, as a function of the number of grid points. Due to the use conservative regridding in the CLM tools, the interpolation errors are small and ice mask areas have less than 1.5% errors relative to the raw ice mask dataset. RACMO2.3, however, uses a smaller ice mask, about 3% smaller than the raw ice mask dataset. While Figure 3 suggests integrating quantities over the native ice mask of the six grids would probably not suffer from large errors due to differing ice masks, we seek to compare these integrated quantities with RACMO. Therefore, we have taken the approach of mapping all model fields to the lowest resolution grids and integrating over the respective low resolution ice masks. Due to the sensitivity of mapping errors to grid coordinates (i.e., unstructured or structured), all quantities are evaluated on both the *f19* and *ne30pg2*, the lowest resolution grid for both dycores considered in this study. In addition, two remapping algorithms are used; ESMF conservative and TempestRemap high-order, monotone algorithm. In all, each integrated quantity is evaluated (at most) four times to provide an estimate of uncertainty due to differences in grid coordinates and remapping algorithm.

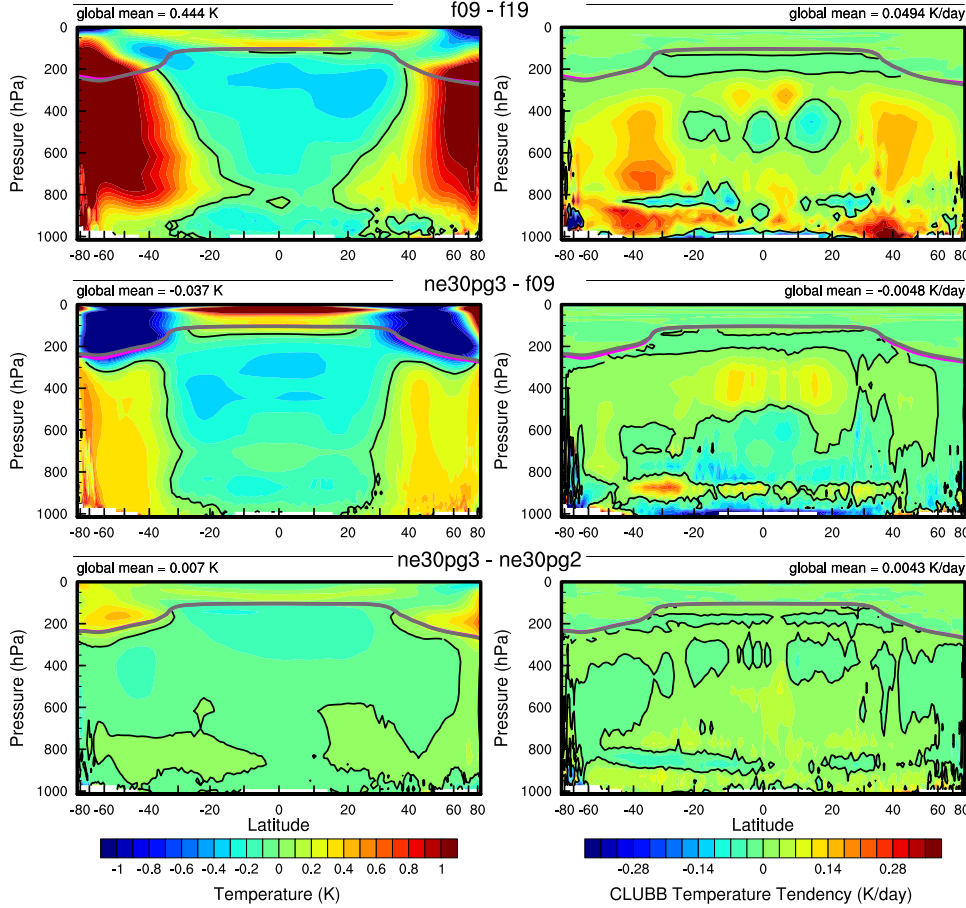
3 Results

3.1 Tropospheric temperatures

Before delving into the simulated characteristics of the Arctic, the global mean differences between the various grids and dycores are assessed. Figure 4 shows plots of the 1979-1998 annual mean, zonal mean height expressed as differences between the uniform resolution grids and dycores. The *f09* grid is warmer than the *f19* grid, primarily in the mid-to-high latitudes and throughout the depth of the troposphere. This is a common response to increasing horizontal resolution in GCMs (Pope & Stratton, 2002; Roeckner et al., 2006), and (A. R. Herrington & Reed, 2020) has shown that this occurs in CAM due to greater resolved vertical velocities that in turn, facilitate greater condensational heating in the macrophyics routine in CLUBB. The right columns in Figure 4 supports this interpretation, which shows an increase in the climatological CLUBB heating in the mid-latitudes in the *f09* grid.

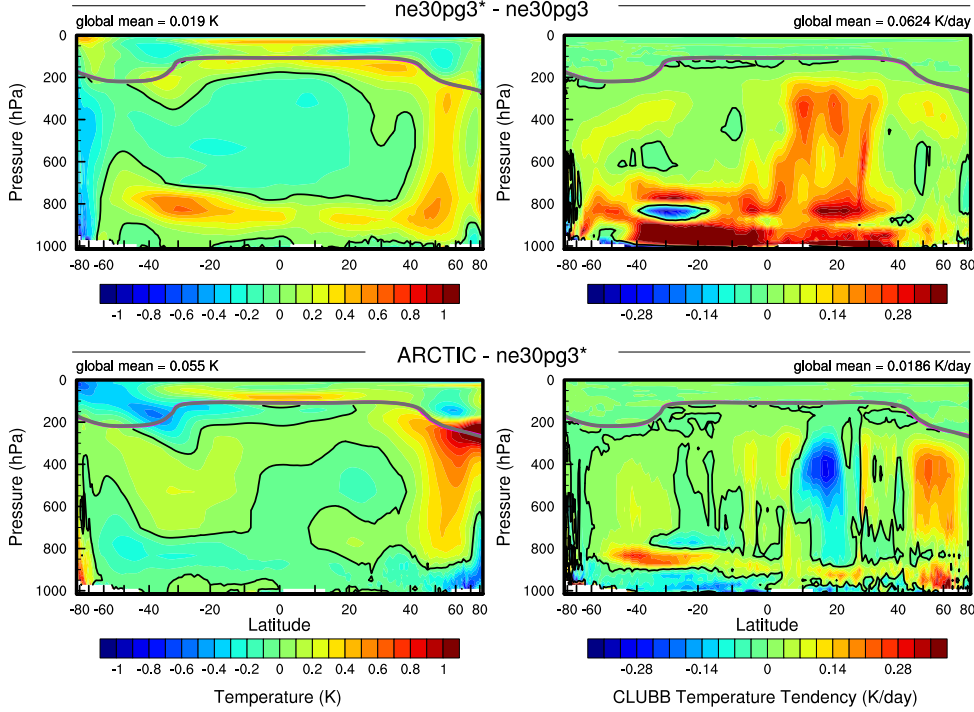
As the SE dycore is less diffusive than the FV dycore, the resolved vertical velocities are larger in the SE dycore, and so a modest, resolution-like sensitivity occurs in which *ne30pg3* is warmer than *f09* (Figure 4). The stratosphere has a different response, in which *ne30pg3* is much cooler than *f09* in the mid-to-high latitudes. The differences in temperature between *ne30pg3* and *ne30pg2* are small, with a slight warming near the tropopause at high latitudes. This is consistent with the similar climates found between these grids in (A. R. Herrington et al., 2019).

Comparing the variable-resolution grids to the uniform resolution grids is complicated because we simultaneously increase the grid resolution and reduce the physics time-step, both of which noticeably impact the solution (D. L. Williamson, 2008). An additional *ne30pg3* simulations is run with the physics time-step used in the *ARCTIC* grid, referred to as *ne30pg3**. Figure 5 shows the change in climatological temperature in zonal-mean height space between *ne30pg3** and *ne30pg3*. A similar warming response to increasing resolution occurs when the time-step is reduced, and the mechanism is similar in that the shorter time-step facilitates greater condensational heating by CLUBB. Figure 5 shows the difference in climatological temperature between the *ARCTIC* grid and the *ne30pg3** grid. The greater condensational heating and warmer temperatures are confined to the regionally refined region when the impact of physics time-steps is removed from the analysis.

**Figure 4.**

It's useful to understand summer temperature biases, instead of annual means, due to its control on ice/snow melt (Ohmura, 2001; Huybers & Tziperman, 2008). Figure 6 shows the 1979-1998 lower troposphere summer temperature bias relative to ERA5. It is computed from the 500 hPa-1000 hPa geopotential thickness, solving for the layer mean virtual temperature using the hypsometric equation. The results generally track with the analysis of the zonal mean height plots; increasing resolution from *f19* to *f09* leads to a warmer climate, and the 1° spectral-elements grids are warmer than the finite-volume grids. The summer temperatures in the finite-volume grids are persistently colder than ERA5 at high latitudes, whereas the 1° spectral-element grids are warmer than ERA5 at only very high-latitudes, north of 80° . The *ARCTIC* grid has similar summer temperatures to the 1° spectral-element grids, except for a region extending from eastern N. Atlantic to northern Eurasia. The *ARCTICGRIS* grid is warmer than the *ARCTIC* grid over most of the Arctic region, but in particular west of Greenland in the Baffin Island/Hudson Bay region, extending westward to the northern coast of Alaska.

Some of these temperature anomalies may be related to summer shortwave cloud forcing differences across the different grids and dycores. Figure 7 shows the summer shortwave cloud forcing climatology in the runs. The uniform 1° - 2° grids have similar cloud forcing, in the range of -85 to -90 W/m 2 averaged north of 40° latitude. The *ARCTIC* grid has a weaker cloud forcing of about -80 W/m 2 , with less negative cloud forcing over the north pole, and the poleward side of the northern hemisphere land masses. The *ARCTCGRIS*

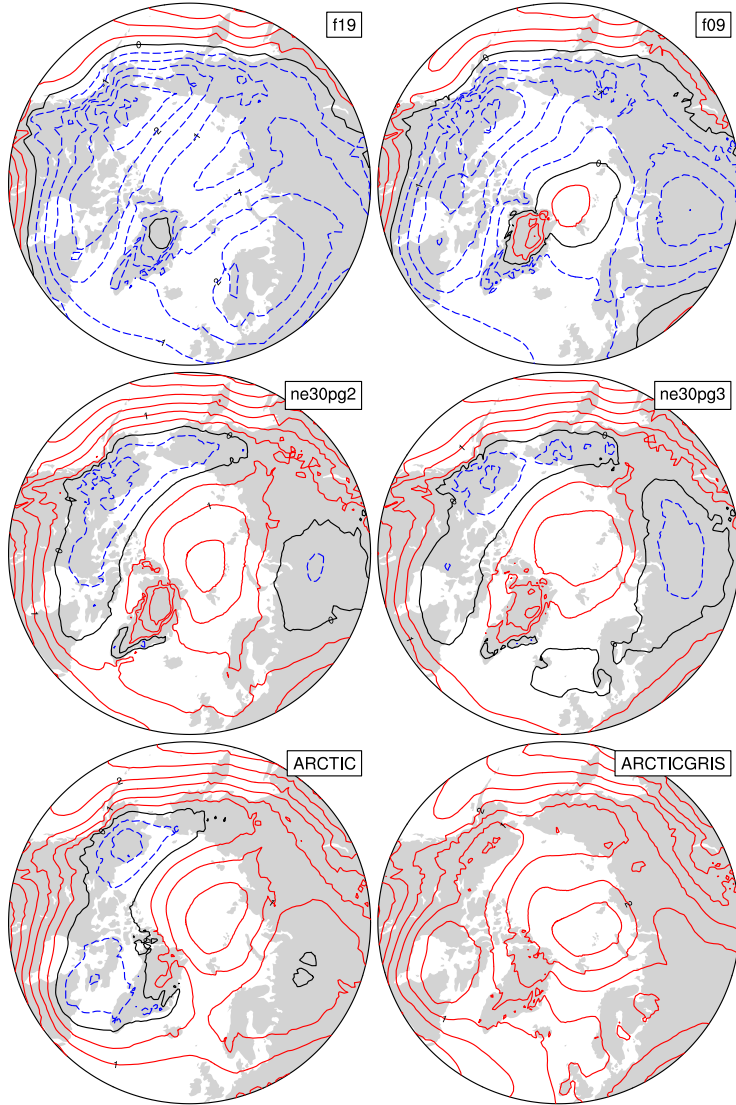
**Figure 5.**

grid has much weaker cloud forcing at -70 W/m^2 , being systematically lower over most of the region plotted. While the cloud forcing to the west of Greenland is reduced in *ARCTCIGRIS*, there are also anomalous southerly winds in this region during summer (not shown), and so the large warm bias to the west of Greenland in Figure 6 is likely a combination of both cloud radiative and circulation changes.

3.2 Greenland surface mass balance

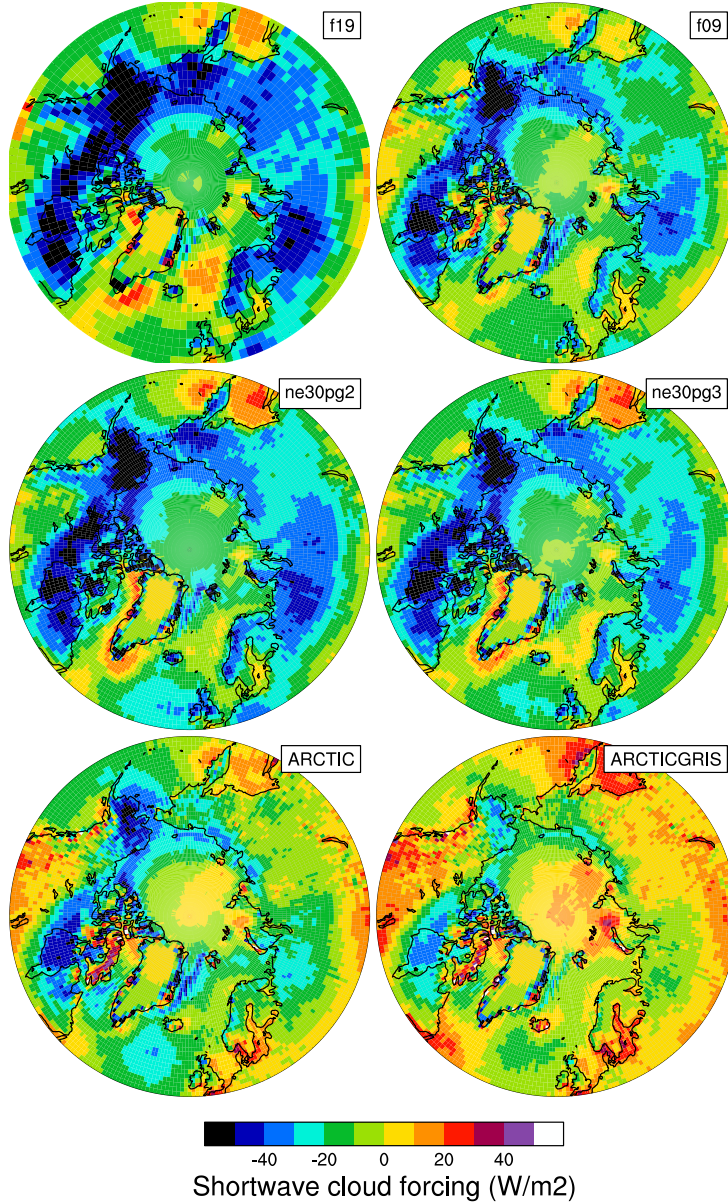
The surface mass balance (SMB) of the Greenland Ice Sheet (GrIS) is simulated in all grids and dycores in this study. As the accuracy of the computed SMB is sensitive to grid resolution, Figure 3 shows the average grid spacing for all six grids in this study. The *ne30pg2* grid has the coarsest representation with an average $\Delta x = 160 \text{ km}$, and the *ARCTICGRIS* grid has the highest resolution with an average $\Delta x = 14.6 \text{ km}$, similar to the grid spacing of the 11 km RACMO model. The *ne30pg3* grid has an average $\Delta x = 111.2 \text{ km}$, which is substantially more coarse than the *f09* grid, having an average $\Delta x = 60 \text{ km}$. This is interesting because *ne30pg3* and *f09* have similar average grid spacing over the entire globe, and comparable computational costs, but due to the convergence of meridians the finite-volume model has enhanced resolution over GrIS. The *ARCTIC* grid has an average grid spacing over GrIS of $\Delta x = 27.8 \text{ km}$, and is about 10 times more expensive than the 1° models. The *ARCTICGRIS* grid is about twice as expensive as the *ARCTIC* grid.

The climatological mean precipitation bias over GrIS is shown in Figure 3, defined as differences from the RACMO2.3p2 5.5km solution (Noël et al., 2019). What sticks out is that the uniform $1^\circ - 2^\circ$ grids have positive bias centered over the southern dome. The *ARCTIC* runs improves this bias substantially, and is all but eliminated in *ARCTCIGRIS* run. The southern dome bias is therefore due to inadequate horizontal resolution, which

**Figure 6.** .

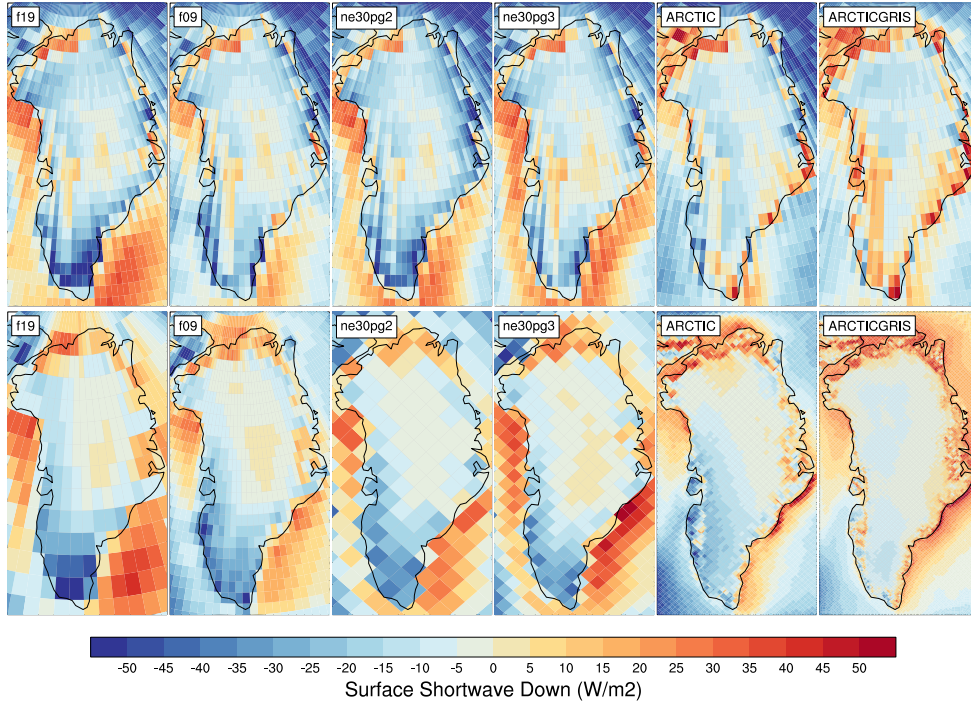
is consistent with the results of (van Kampenhout et al., 2018). Southeast Greenland has the largest accumulation rates in GrIS due to synoptic systems moving in from the southeast, which become orographically lifted by the steep southeast ice sheet margin, dumping large amounts of precipitation along the southeast coast. At lower horizontal resolutions, the topography is too smooth and large amounts of moisture penetrates further inland, incorrectly dumping large amounts of precipitation onto the interior of the ice sheet.

Figure 10 shows time-series of integrated precipitation and snow/ice melt over the GrIS in the various different grids and dycores, with both RACMO2.3 and 2.3p2 show in black. The 1979-1998 climatological mean values are provided as circles on the right side of the panels. The uniform 1° - 2° grids all show a distinctive positive bias in precipitation due to this over-prediction of interior precipitation rates. The variable-resolution grids have the smallest precipitation biases, providing a comparable solution to RACMO. The *f19* and *f09* perform similarly, with +110 Gt/yr bias, whereas *ne30pg3*

**Figure 7.**

is biased by about +170 Gt/yr and *ne30pg2*, +230 Gt/yr. The results suggest that uniform resolution spectral-element grids have larger biases than the finite-volume grids, consistent with spectral-element grids having a coarser representation of GrIS (Figure 3). While it seems likely that *ne30pg2* has the largest bias of all the grids, it's difficult to say for certain that the *ne30pg3* precipitation biases are worse than the finite-volume grids, owing to the use of a single realization for each grid.

The combined snow/ice melt integrated over the GrIS is given by the bottom panel of Figure 10. The *ARCTIC* grid simulates the most realistic melt rates, with all other grids tending to have larger melt rates than RACMO. The *ARCTICGRIS* grid over-predicts melting by about 150 Gt/yr. This is likely due to an anomalously warm lower troposphere during the summer, relative to the *ARCTIC* run (not shown). The *f19* and

**Figure 8.** .

354 f09 melting rates are improved over *ARCTICGRIS*, with a positive melt bias between
 355 70-90 Gt/yr. The spectral-element grids have the largest positive melt bias, between 210-
 356 230 Gt/yr.

357 Figure 11 shows the distribution of point-wise differences from LIVVkit observational
 358 database, as a violin plot. The IceBridge dataset is exclusively from the interior
 359 of the ice sheet and represents accumulation rates. The uniform 1° - 2° grids have sim-
 360 ilar median errors of about +35-50 mm.w.e, while the variable-resolution errors are no-
 361 ticeably smaller. The in-situ observations in the accumulation zone, shown in the mid-
 362 dle plot looks very similar to the IceBridge errors, and so provides confidence that the
 363 variable-resolution grids are outperforming the uniform grids in the interior accumula-
 364 tion zone. The errors evaluated at in-situ ablation zone measurements are in tension with
 365 the RACMO results in Figure 10. They indicate that the uniform 1° - 2° grids perform
 366 similarly, the *ARCTIC* grid showing a reduction in bias and the *ARCTICGRIS* hav-
 367 ing the smallest bias of all grids. However, the in-situ ablation measurements are sparse
 368 in time and space, and so there is a large amount of uncertainty in extending these re-
 369 sults to the entirety of the ablation zone.

370 The infamous k-transect mass balance profile is contained in the LIVVkit database,
 371 and shown in Figure 12, along with all the simulations. The in-situ observation points
 372 seem to be nicely replicated by the *ARCTICGRIS* run, whereas the *ARCTIC* grid seems
 373 to be biased positive in the higher-elevations of the ablation zone. The f09 grid is surpris-
 374 ingly competitive with the variable-resolution grids, capturing a realistic slope of the elevation-
 375 SMB curve. The elevation-SMB slopes of the uniform spectral-element and f19 grid are
 376 too shallow, in particular at the higher elevation regions of the k-transect. Figure ?? shows
 377 the representation of the surface of the ice sheet along these transects in the simulations,
 378 compared to a high resolution elevation dataset. The 1° - 2° grids are noticeably coarse,
 379 with only a handful of grid cells populating the transect. The f09 grid is a bit of an ex-

ception. The *f*09 grid cells become very narrow in the meridional direction at high latitudes, and so a larger number of grid cells can populate the east-west transect, consistent with its skillful representation of the ablation zone compared with RACMO.

What the authors refer to as the “b-transect” in northwest Greenland (Figure 12) is characterized by orographic precipitation, resulting in the accumulation zone extending down to the ice margin. The variable resolution grids perform relatively well, with larger SMBs at lower elevations where the precipitation rates are highest, whereas the $1^\circ - 2^\circ$ grids underestimate the SMB in these lower elevation regions. Only the variable resolution grids can capture the local reduction in SMB in the 1500-2000 m region. The skill of the variable-resolution grids is clearly related to the accurate representation of this steep transect, while also capturing the protrusion around 1500-2000 m that coincides with the local minimum in SMB (Figure ??).

3.3 Impact of horizontal resolution on extremes

Synoptic storms are identified and analyzed using TempestExtremes (Ullrich et al., 2021). The new *ARCTIC* grid contains $\frac{1}{4}^\circ$ refinement north of about 45° latitude, and so the storm tracker is applied to this region for the *ARCTIC* and *ne30pg3* run to identify differences in storm characteristics due to horizontal resolution. Figure 14 shows the mean precipitation rates averaged over all January storms identified by TempestExtremes. The iconic comma structure of the mid-latitude cyclones is simulated in *ne30pg3* and *ARCTIC* grids, with the magnitudes about the same in these two grids, with perhaps a marginal increase in precipitation rates in the storm center of the *ARCTIC* grid. For good measure, the *ne30pg3** run is also plotted, and looks more-or-less identical to the *ne30pg3* run.

As has been previously reported, horizontal resolution can have large impacts on extreme precipitation events. Figure 15 is a PDF of the precipitation rates associated with synoptic storms, by month. The *ARCTIC* run has larger extreme precipitation rates compared to *ne30pg3* in every month, but the increase is greatest in the summer months, which coincides with the most extreme events of the year. This is primarily due to an increase in resolution; the *ne30pg3** only marginally increases the precipitation rates compared with *ne30pg3*. The *f*09 and *f*19 grids look similar to *ne30pg3*, but with *f*09 having more frequent extreme precipitation events than *f*19 (not shown). It should also be noted that the PDFs are evaluated on an identical composite grid for all runs, and so storm statistics are not impacted by differences in output resolution.

The extreme precipitation rates in the *ARCTIC* run are closer to the ERA5 reanalysis than in *ne30pg3* (Figure 15). It’s difficult to know the extent that the extreme precipitation rates in ERA5 are constrained by data assimilation, or whether these precipitation rates are due to using a similar $\frac{1}{4}^\circ$ model as the *ARCTIC* grid. However, precipitation rates in $\frac{1}{4}^\circ$ models tend to produce more skillful extreme events (O’Brien et al., 2016).

3.4 Orographic gravity waves emanating from Greenland

3.5 Katabatic winds emanating from Greenland

4 Conclusions

Acknowledgments

This material is based upon work supported by the National Center for Atmospheric Research (NCAR), which is a major facility sponsored by the NSF under Cooperative Agreement 1852977. Computing and data storage resources, including the Cheyenne super-

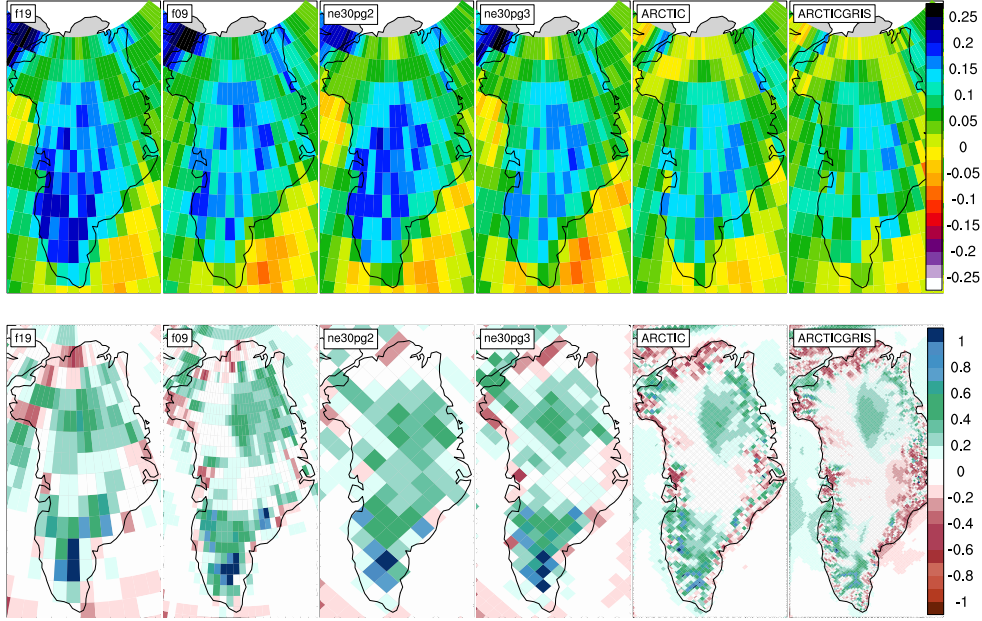


Figure 9. Climatological (1979-1998) annual precipitation rate bias (in mm/yr) relative to the RACMO2.3p2 5.5km resolution data product (Noël et al., 2019).

426 computer (doi:10.5065/D6RX99HX), were provided by the Computational and Information
427 Systems Laboratory (CISL) at NCAR.

428 The data presented in this manuscript is available at <https://github.com/adamrher/2020-arcticgrids>.
429

430 References

- 431 Beljaars, A., Brown, A., & Wood, N. (2004). A new parametrization of turbulent
432 orographic form drag. *Quart. J. Roy. Meteor. Soc.*, *130*(599), 1327–1347. doi:
433 10.1256/qj.03.73
- 434 Bogenschutz, P. A., Gettelman, A., Morrison, H., Larson, V. E., Craig, C., & Scha-
435 nen, D. P. (2013). Higher-order turbulence closure and its impact on climate
436 simulations in the community atmosphere model. *Journal of Climate*, *26*(23),
437 9655–9676.
- 438 Bromwich, D. H., Cassano, J. J., Klein, T., Heinemann, G., Hines, K. M., Steffen,
439 K., & Box, J. E. (2001). Mesoscale modeling of katabatic winds over greenland
440 with the polar mm5. *Monthly Weather Review*, *129*(9), 2290–2309.
- 441 Canuto, C., Hussaini, M. Y., Quarteroni, A., & Zang, T. (2007). *Spectral methods:*
442 *Evolution to complex geometries and applications to fluid dynamics* (1st ed.).
443 Springer.
- 444 Collins, W. D., Rasch, P. J., Boville, B. A., Hack, J. J., McCaa, J. R., Williamson,
445 D. L., ... Zhang, M. (2006). The formulation and atmospheric simulation
446 of the community atmosphere model version 3 (cam3). *Journal of Climate*,
447 *19*(11), 2144–2161.
- 448 Dennis, J. M., Edwards, J., Evans, K. J., Guba, O., Lauritzen, P. H., Mirin, A. A.,
449 ... Worley, P. H. (2012). CAM-SE: A scalable spectral element dynamical
450 core for the Community Atmosphere Model. *Int. J. High. Perform. C.*, *26*(1),
451 74–89. Retrieved from <http://hpc.sagepub.com/content/26/1/74.abstract>

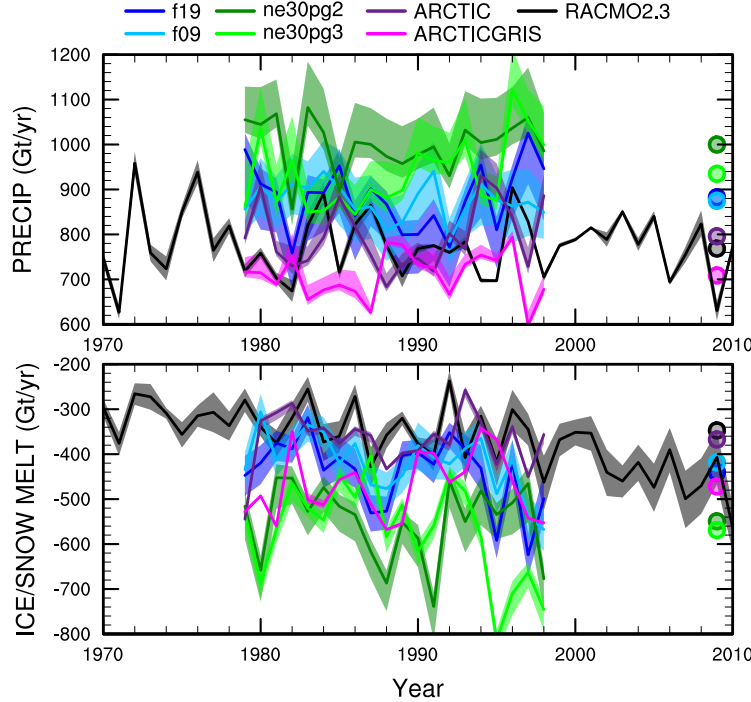
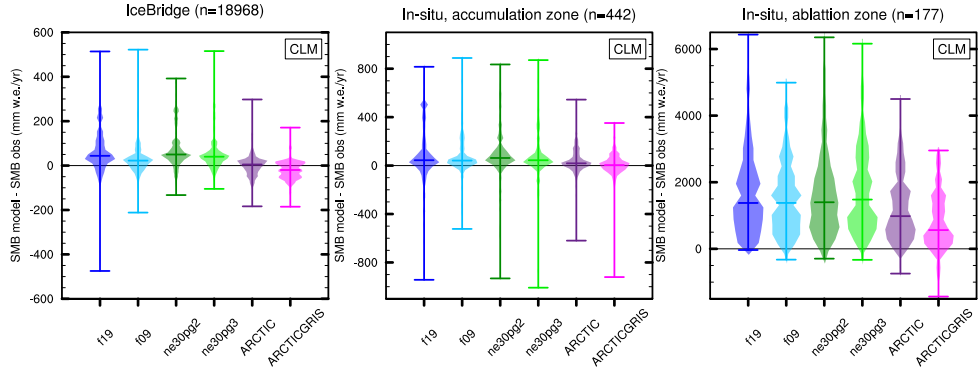
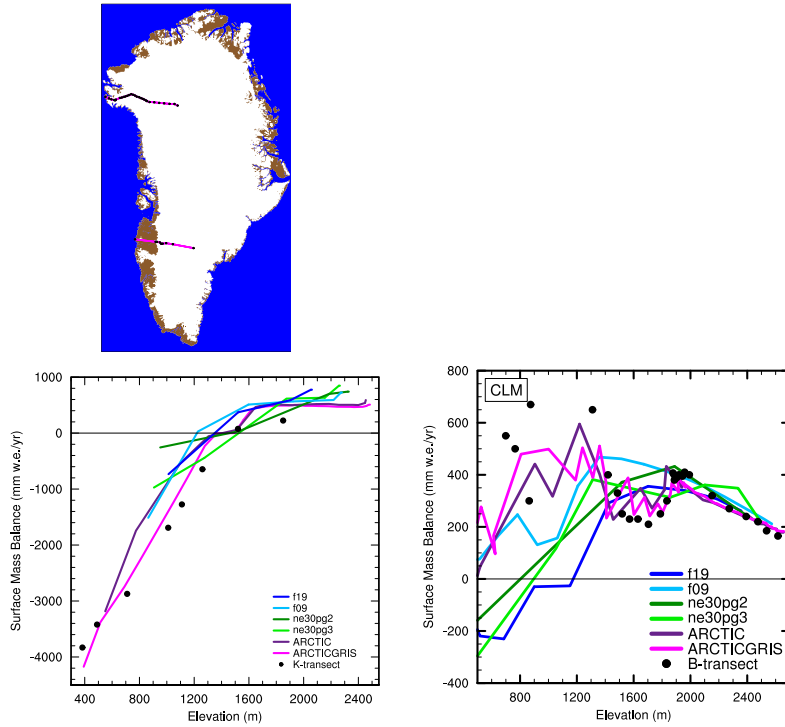
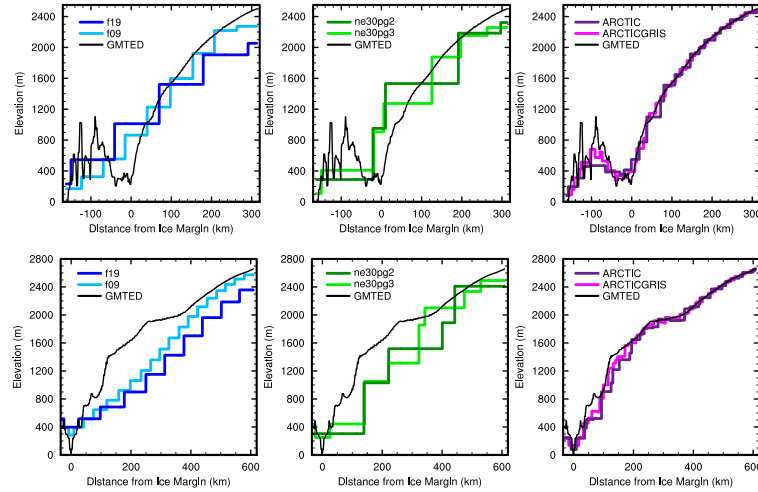
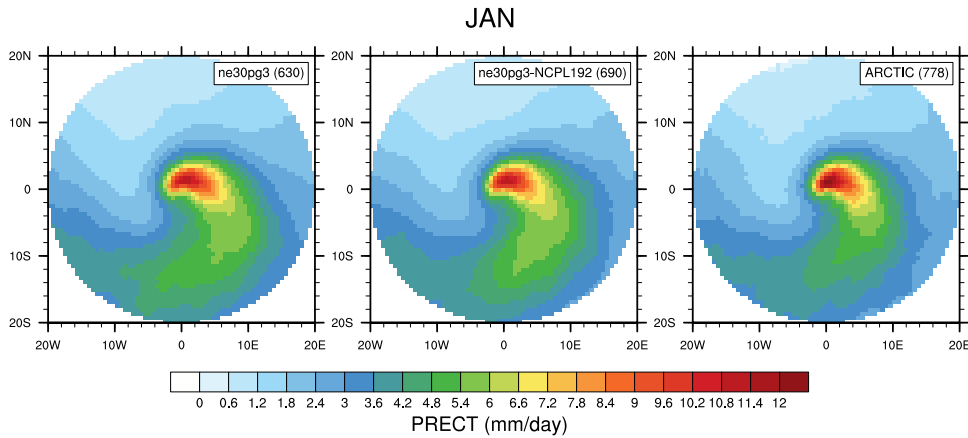


Figure 10. Time-series of annual (solid+liquid) precipitation (top) and annual runoff (bottom) integrated over the Greenland Ice Sheet for all six simulations and compared to RACMO3.2. The raw fields are mapped to two target low resolution grids, f19 & ne30pg2, and using two different remapping methods, conservative ESMF and high order TempestRemap. The remapped values are then integrated over the ice mask of the target grid. This gives four time-series for each simulation (three for f19 & ne30pg2), with the mean value given by the solid line and shading spanning the extent of the remapped solutions.

- doi: 10.1177/1094342011428142
 Evans, K. J., Kennedy, J. H., Lu, D., Forrester, M. M., Price, S., Fyke, J., ... others (2019). Livvkit 2.1: automated and extensible ice sheet model validation. *Geoscientific Model Development*, 12(3), 1067–1086.
 Gettelman, A., Morrison, H., Santos, S., Bognenschutz, P., & Caldwell, P. (2015). Advanced two-moment bulk microphysics for global models. part ii: Global model solutions and aerosol–cloud interactions. *Journal of Climate*, 28(3), 1288–1307.
 Golaz, J.-C., Larson, V. E., & Cotton, W. R. (2002). A pdf-based model for boundary layer clouds. part i: Method and model description. *Journal of the Atmospheric Sciences*, 59(24), 3540–3551. doi: 10.1175/1520-0469(2002)059<3540:apbmfb>2.0.co;2
 Guba, O., Taylor, M. A., Ullrich, P. A., Overfelt, J. R., & Levy, M. N. (2014). The spectral element method (sem) on variable-resolution grids: evaluating grid sensitivity and resolution-aware numerical viscosity. *Geosci. Model Dev.*, 7(6), 2803–2816. doi: 10.5194/gmd-7-2803-2014
 Guo, Z., Wang, M., Qian, Y., Larson, V. E., Ghan, S., Ovchinnikov, M., ... Zhou, T. (2015). Parametric behaviors of clubb in simulations of low clouds in the community atmosphere model (cam). *Journal of Advances in Modeling Earth Systems*, 7(3), 1005–1025.

**Figure 11.****Figure 12.**

- 472 Herrington, A., Lauritzen, P., Taylor, M. A., Goldhaber, S., Eaton, B. E., Bacmeis-
 473 ter, J., ... Ullrich, P. (2018). Physics-dynamics coupling with element-based
 474 high-order galerkin methods: quasi equal-area physics grid. *Mon. Wea. Rev.*,
 475 47, 69–84. doi: 10.1175/MWR-D-18-0136.1
- 476 Herrington, A., & Reed, K. (2018). An idealized test of the response of the commu-
 477 nity atmosphere model to near-grid-scale forcing across hydrostatic resolutions.
 478 *J. Adv. Model. Earth Syst.*, 10(2), 560–575.
- 479 Herrington, A. R., Lauritzen, P. H., Reed, K. A., Goldhaber, S., & Eaton, B. E.
 480 (2019). Exploring a lower resolution physics grid in cam-se-cslam. *Journal of*
 481 *Advances in Modeling Earth Systems*, 11.
- 482 Herrington, A. R., & Reed, K. A. (2020). On resolution sensitivity in the commu-
 483 nity atmosphere model. *Quarterly Journal of the Royal Meteorological Society*,

**Figure 13.****Figure 14.**

484

146(733), 3789–3807.

485

Hurrell, J. W., Hack, J. J., Shea, D., Caron, J. M., & Rosinski, J. (2008). A new sea surface temperature and sea ice boundary dataset for the community atmosphere model. *Journal of Climate*, 21(19), 5145–5153.

486

Huybers, P., & Tziperman, E. (2008). Integrated summer insolation forcing and 40,000-year glacial cycles: The perspective from an ice-sheet/energy-balance model. *Paleoceanography*, 23(1).

487

Jablonowski, C., & Williamson, D. L. (2006). A baroclinic instability test case for atmospheric model dynamical cores. *Q. J. R. Meteorol. Soc.*, 132, 2943–2975.

488

Jablonowski, C., & Williamson, D. L. (2011). The pros and cons of diffusion, filters and fixers in atmospheric general circulation models., in: P.H. Lauritzen, R.D. Nair, C. Jablonowski, M. Taylor (Eds.), Numerical techniques for global atmospheric models. *Lecture Notes in Computational Science and Engineering*, Springer, 80.

489

Lauritzen, P. H., Bacmeister, J. T., Callaghan, P. F., & Taylor, M. A. (2015). Near global model topography generation software for unstructured grids. *Geoscientific Model Development Discussions*, 8(6), 4623–4651. doi: 10.5194/gmdd-8

490

491

492

493

494

495

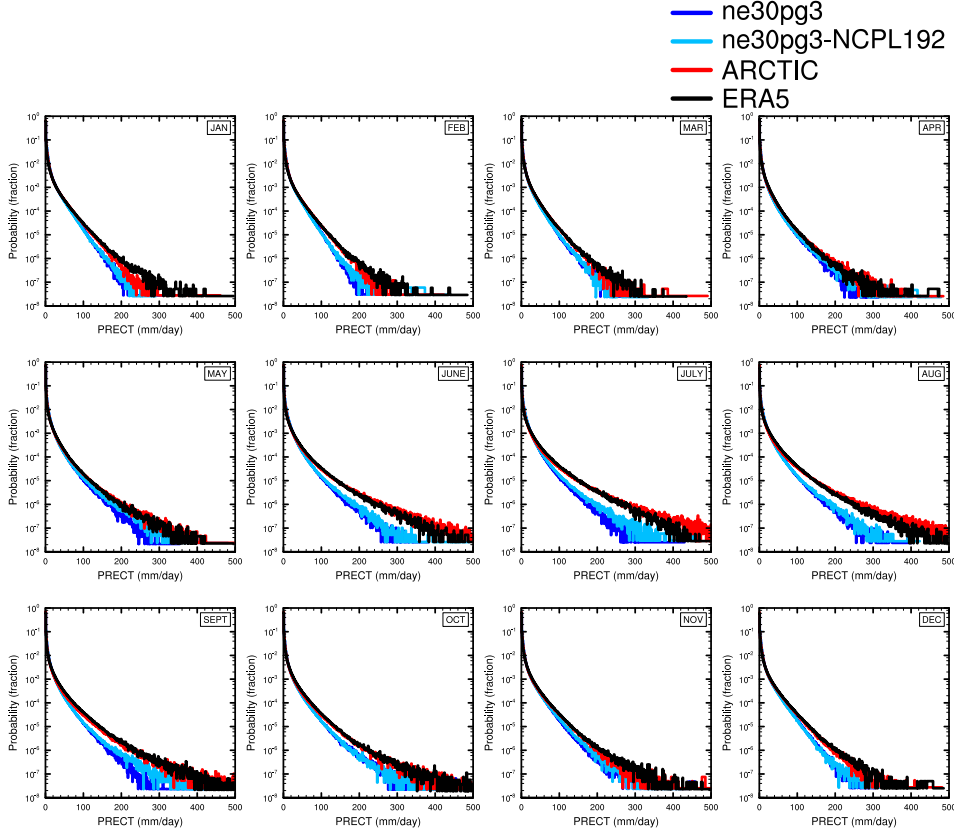
496

497

498

499

500

**Figure 15.** .

501

-4623-2015

502
503
504
505

Lauritzen, P. H., Mirin, A., Truesdale, J., Raeder, K., Anderson, J., Bacmeister, J., & Neale, R. B. (2011). Implementation of new diffusion/filtering operators in the CAM-FV dynamical core. *Int. J. High Perform. Comput. Appl.*. doi: 10.1177/10943432011410088

506
507
508
509
510

Lauritzen, P. H., Nair, R., Herrington, A., Callaghan, P., Goldhaber, S., Dennis, J., ... Dubos, T. (2018). NCAR CESM2.0 release of CAM-SE: A reformulation of the spectral-element dynamical core in dry-mass vertical coordinates with comprehensive treatment of condensates and energy. *J. Adv. Model. Earth Syst.*. doi: 10.1029/2017MS001257

511
512
513
514

Lauritzen, P. H., Taylor, M. A., Overfelt, J., Ullrich, P. A., Nair, R. D., Goldhaber, S., & Kelly, R. (2017). CAM-SE-CSLAM: Consistent coupling of a conservative semi-lagrangian finite-volume method with spectral element dynamics. *Mon. Wea. Rev.*, 145(3), 833-855. doi: 10.1175/MWR-D-16-0258.1

515
516

Lin, S.-J. (2004). A 'vertically Lagrangian' finite-volume dynamical core for global models. *Mon. Wea. Rev.*, 132, 2293-2307.

517
518

Lin, S.-J., & Rood, R. B. (1997). An explicit flux-form semi-Lagrangian shallow-water model on the sphere. *Q.J.R.Meteorol.Soc.*, 123, 2477-2498.

519
520
521
522
523

Lofverstrom, M., Fyke, J. G., Thayer-Calder, K., Muntjewerf, L., Vizcaino, M., Sacks, W. J., ... Bradley, S. L. (2020). An efficient ice sheet/earth system model spin-up procedure for cesm2-cism2: Description, evaluation, and broader applicability. *Journal of Advances in Modeling Earth Systems*, 12(8), e2019MS001984.

- 524 Neale, R. B., Richter, J. H., & Jochum, M. (2008). The impact of convection on
 525 ENSO: From a delayed oscillator to a series of events. *J. Climate*, *21*, 5904-
 526 5924.
- 527 Noël, B., Van De Berg, W., Van Meijgaard, E., Kuipers Munneke, P., Van De Wal,
 528 R., & Van Den Broeke, M. (2015). Evaluation of the updated regional climate
 529 model racmo2. 3: summer snowfall impact on the greenland ice sheet. *The
 530 Cryosphere*, *9*(5), 1831–1844.
- 531 Noël, B., van de Berg, W. J., Lhermitte, S., & van den Broeke, M. R. (2019). Rapid
 532 ablation zone expansion amplifies north greenland mass loss. *Science advances*,
 533 *5*(9), eaaw0123.
- 534 O'Brien, T. A., Collins, W. D., Kashinath, K., Rübel, O., Byna, S., Gu, J., ...
 535 Ullrich, P. A. (2016). Resolution dependence of precipitation statistical
 536 fidelity in hindcast simulations. *J. Adv. Model. Earth Syst.*, *8*(2), 976–
 537 990. Retrieved from <http://dx.doi.org/10.1002/2016ms000671> doi:
 538 10.1002/2016ms000671
- 539 Ohmura, A. (2001). Physical basis for the temperature-based melt-index method.
 540 *Journal of applied Meteorology*, *40*(4), 753–761.
- 541 Pope, V., & Stratton, R. (2002). The processes governing horizontal resolution sensi-
 542 tivity in a climate model. *Climate Dynamics*, *19*(3-4), 211–236.
- 543 Putman, W. M., & Lin, S.-J. (2007). Finite-volume transport on various cubed-
 544 sphere grids. *J. Comput. Phys.*, *227*(1), 55-78.
- 545 Richter, J. H., Sassi, F., & Garcia, R. R. (2010). Toward a physically based gravity
 546 wave source parameterization in a general circulation model. *J. Atmos. Sci.*,
 547 *67*, 136-156. doi: dx.doi.org/10.1175/2009JAS3112.1
- 548 Roeckner, E., Brokopf, R., Esch, M., Giorgetta, M., Hagemann, S., Kornblueh, L.,
 549 ... Schulzweida, U. (2006). Sensitivity of simulated climate to horizontal
 550 and vertical resolution in the echam5 atmosphere model. *Journal of Climate*,
 551 *19*(16), 3771–3791.
- 552 Sellevold, R., Van Kampenhout, L., Lenaerts, J., Noël, B., Lipscomb, W. H., &
 553 Vizcaino, M. (2019). Surface mass balance downscaling through elevation
 554 classes in an earth system model: Application to the greenland ice sheet. *The
 555 Cryosphere*, *13*(12), 3193–3208.
- 556 Smirnova, J., & Golubkin, P. (2017). Comparing polar lows in atmospheric reanal-
 557 yses: Arctic system reanalysis versus era-interim. *Monthly Weather Review*,
 558 *145*(6), 2375–2383.
- 559 Stocker, T. (2014). *Climate change 2013: the physical science basis: Working group
 560 i contribution to the fifth assessment report of the intergovernmental panel on
 561 climate change*. Cambridge university press.
- 562 Suarez, M. J., & Takacs, L. L. (1995). Volume 5 documentation of the aries/geos dy-
 563 namical core: Version 2.
- 564 Taylor, M. A., Tribbia, J., & Iskandarani, M. (1997). The spectral element method
 565 for the shallow water equations on the sphere. *J. Comput. Phys.*, *130*, 92-108.
- 566 Ullrich, P. A., Zarzycki, C. M., McClenney, E. E., Pinheiro, M. C., Stansfield, A. M.,
 567 & Reed, K. A. (2021). Tempestextremes v2. 1: a community framework for
 568 feature detection, tracking and analysis in large datasets. *Geoscientific Model
 569 Development Discussions*, 1–37.
- 570 van Kampenhout, L., Lenaerts, J. T., Lipscomb, W. H., Lhermitte, S., Noël, B.,
 571 Vizcaíno, M., ... van den Broeke, M. R. (2020a). Present-day greenland
 572 ice sheet climate and surface mass balance in cesm2. *Journal of Geophysical
 573 Research: Earth Surface*, *125*(2), e2019JF005318.
- 574 van Kampenhout, L., Lenaerts, J. T., Lipscomb, W. H., Lhermitte, S., Noël, B.,
 575 Vizcaíno, M., ... van den Broeke, M. R. (2020b). Present-day greenland
 576 ice sheet climate and surface mass balance in cesm2. *Journal of Geophysical
 577 Research: Earth Surface*, *125*(2).
- 578 van Kampenhout, L., Rhoades, A. M., Herrington, A. R., Zarzycki, C. M., Lenaerts,

- 579 J. T. M., Sacks, W. J., & van den Broeke, M. R. (2018). Regional grid refine-
580 ment in an earth system model: Impacts on the simulated greenland surface
581 mass balance. *The Cryosphere Discuss.*. doi: 10.5194/tc-2018-257
- 582 Williamson, D. (2007). The evolution of dynamical cores for global atmospheric
583 models. *J. Meteor. Soc. Japan*, 85, 241-269.
- 584 Williamson, D. L. (2008). Convergence of aqua-planet simulations with increas-
585 ing resolution in the community atmospheric model, version 3. *Tellus A*, 60(5),
586 848–862. doi: 10.1111/j.1600-0870.2008.00339.x
- 587 Zhang, G., & McFarlane, N. (1995). Sensitivity of climate simulations to the pa-
588 rameterization of cumulus convection in the canadian climate centre general
589 circulation model. *Atmosphere-ocean*, 33(3), 407-446.